5984 *Biochemistry* **2009,** *48,* 5984–5993
DOI: 10.1021/bi900270w

BIOCHEMISTRY
including biophysical chemistry & molecular biology
Article

Redox-Dependent Dynamics of a Dual Thioredoxin Fold Protein: Evolution of Specialized Folds[†]

Andrea Hall,[‡] Derek Parsonage,[§] David Horita,[§] P. Andrew Karplus,[‡] Leslie B. Poole,[§] and Elisar Barbar*[,‡]

[‡]*Department of Biochemistry and Biophysics, Oregon State University, Corvallis, Oregon 97331, and* [§]*Department of Biochemistry, Wake Forest University School of Medicine, Winston-Salem, North Carolina 27157*

Received February 17, 2009; Revised Manuscript Received April 28, 2009

ABSTRACT: An enzyme system protecting bacteria from oxidative stress includes the flavoprotein AhpF and the peroxiredoxin AhpC. The N-terminal domain of AhpF (NTD), with two fused thioredoxin (Trx) folds, belongs to the hyperthermophilic protein disulfide oxidoreductase family. The NTD is distinct in that it contains a redox active ***a*** fold with a CxxC sequence and a redox inactive ***b*** fold that has lost the CxxC motif. Here we characterize the stability, the ^{15}N backbone relaxation, and the hydrogen−deuterium exchange properties of reduced [NTD-$(SH)_2$] and oxidized (NTD-S_2) NTD from *Salmonella typhimurium*. While both NTD-$(SH)_2$ and NTD-S_2 exhibit similar equilibrium unfolding transitions and order parameters, R_{ex} relaxation terms are quite distinct with considerably more intermediate time scale motions in NTD-S_2. Hydrogen exchange protection factors show that the slowly exchanging core corresponds to residues in the ***b*** fold in both NTD-$(SH)_2$ and NTD-S_2. Interestingly, folded-state dynamic fluctuations in the catalytic ***a*** fold are significantly increased for residues in NTD-S_2 compared to NTD-$(SH)_2$. Taken together, these data demonstrate that oxidation of the active site disulfide does not significantly increase stability but results in a dramatic increase in conformational heterogeneity in residues primarily in the redox active ***a*** fold. Differences in dynamics between the two folds of the NTD suggest that each evolved a specialized function which, in the ***a*** fold, couples redox state to internal motions which may enhance catalysis and specificity and, in the ***b*** fold, provides a redox insensitive stable core.

The N-terminal domain of the flavoprotein AhpF (NTD)[1] is composed of two fused and intimately interacting thioredoxin (Trx) folds. The NTD is part of a system that provides protection from oxidative stress in bacteria (*1*−*3*) by catalyzing the reduction of hydrogen peroxide and organic hydroperoxides to their corresponding alcohol and water. Two enzymes are required: AhpC, a bacterial peroxiredoxin (Prx) (*4*), and AhpF, a flavoenzyme disulfide reductase. In addition to the NTD, AhpF contains a thioredoxin reductase (TrxR)-like domain (*3*, *5*, *6*) (Figure 1).

The NTD acts as an appended substrate for the TrxR-like portion of AhpF (*6*−*8*) and is a highly specific and effective reductant of AhpC (*3*). A single redox active disulfide (-Cys_{129}-His-Asn-Cys_{132}-), characteristic of Trx-like proteins, is located in the C-terminal Trx fold and provides redox activity, while the N-terminal Trx fold has no such motif and is thus inactive in redox reactions (Figure 2). Using nomenclature for Trx-like domains in other proteins (*9*, *10*), we refer to the redox active C-terminal fold as the ***a*** fold and the redox inactive N-terminal fold as the ***b*** fold. In addition to the CxxC motif, the active site of the ***a*** fold makes use of a conserved glutamic acid from the ***b*** fold that reaches across the interface of the two folds. Sequence and structural comparisons indicate that the NTD is a subgroup of the protein disulfide oxidoreductase (PDO) family of proteins important for redox chemistry and isomerization in Archaea (*11*). A PDO-like protein present in hyperthermophilic organisms is thought to represent an intermediate in the evolution of the NTD (*5*, *12*) (Figure 2C).

A construct of the NTD (residues 1−202 of AhpF) retains the function (*7*) and structure (*13*) of the NTD in the full AhpF (residues 1−521) and provides an excellent model for high-resolution structure−function characterization of a redox active protein in solution. To determine if and how the two Trx folds of

[†]This study was supported by a grant from the National Institutes of Health to L.B.P. with a subcontract to P.A.K. and E.B. (RO1 GM050389). The nucleic acid and protein core and the mass spectrometry facilities and services core were supported by the OSU Environmental Health Sciences Center (P30 ES000210).

*To whom correspondence should be addressed: Department of Biochemistry and Biophysics, Oregon State University, Corvallis, OR 97331. Telephone: (541) 737-4143. Fax: (541) 737-0481. E-mail: barbare@science.oregonstate.edu.

[1]Abbreviations: AhpR, alkyl hydroperoxide reductase; AhpF, alkyl hydroperoxide reductase F component (flavoprotein reductase); AhpC, alkyl hydroperoxide reductase C component (peroxidase); *St*AhpF, *Salmonella typhimurium* AhpF; *St*AhpC, *S. typhimurium* AhpC; NTD, N-terminal domain (residues 1−202) of *St*AhpF; NTD-S_2, oxidized NTD; NTD-$(SH)_2$, reduced NTD; TrxR, thioredoxin reductase; Trx, thioredoxin; *Ec*Trx, *Escherichia coli* Trx; Prx, peroxiredoxin; HSQC, heteronuclear single-quantum correlation; NOE, nuclear Overhauser effect; H−D exchange, hydrogen−deuterium exchange; DTT, 1,4-dithiothreitol; CD, circular dichroism; DSS, 2,2-dimethyl-2-silapentane-5-sulfonate sodium salt; βME, β-mercaptoethanol; PDB, Protein Data Bank.

 Published on Web 05/21/2009

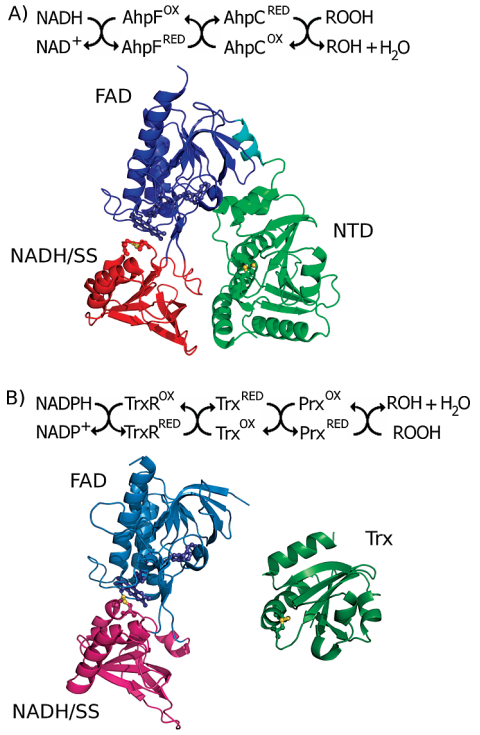

FIGURE 1: Two pathways for the reduction of peroxides by flavoproteins. (A) The bacterial AhpF/AhpC system (also known as the alkyl hydroperoxide reductase system) uses the two enzymes AhpF and AhpC to reduce hydrogen peroxide and organic hydroperoxides using NADH. A ribbon diagram of AhpF (PDB entry 1HYU), depicting only one subunit of the dimer, is shown. (B) The TrxR/Trx/Prx system is analogous to the AhpF/AhpC system. Ribbon diagrams of TrxR (PDB entry 1TDE) and Trx (PDB entry 2TRX) are shown. A comparison of the proteins in the two systems reveals that AhpF consists of a fused TrxR-like domain and a Trx-like domain. To highlight this homology, the same coloring scheme is used in both panels A and B with red and blue shades for the FAD binding (FAD) and the NADH binding redox active disulfide-containing (NADH/SS) domains of the TrxR(-like) protein, respectively, and green shades for the Trx(-like) protein/domain. The N-terminal domain in AhpF (NTD) is made up of two interacting Trx folds and acts like an appended substrate for the TrxR-like domain of AhpF (linker region colored cyan). The bound FAD molecule and redox active cysteines in both panels A and B are shown as ball-and-stick diagrams with sulfur atoms colored yellow.

the NTD function as a single unit and to gain insight into changes that occur with oxidation in this class of Trx-related proteins, we have analyzed the dynamics and stability of the reduced [NTD-$(SH)_2$] and oxidized (NTD-S_2) NTD from *Salmonella typhimurium*. Our results indicate that the two Trx folds behave as a single cooperative folding unit but have distinct dynamic properties not detected in crystal structures. Each fold has a specialized function such that the ***b*** fold provides protein stability in both redox states while the ***a*** fold is more dynamic and shows redox-state-specific changes in dynamics; upon oxidation, residues in the ***a*** fold show increased internal flexibility and conformational heterogeneity. From these analyses, we propose that protein dynamics are adaptable features in the evolutionary divergence of the broader Trx-like family.

MATERIALS AND METHODS

Protein Preparation. All buffers and stock solutions were freshly prepared. The unlabeled NTD was expressed and purified as previously described (*7*). The uniformly ^{15}N-labeled NTD was expressed from pAF[1-202] (*7*) in *Escherichia coli* strain

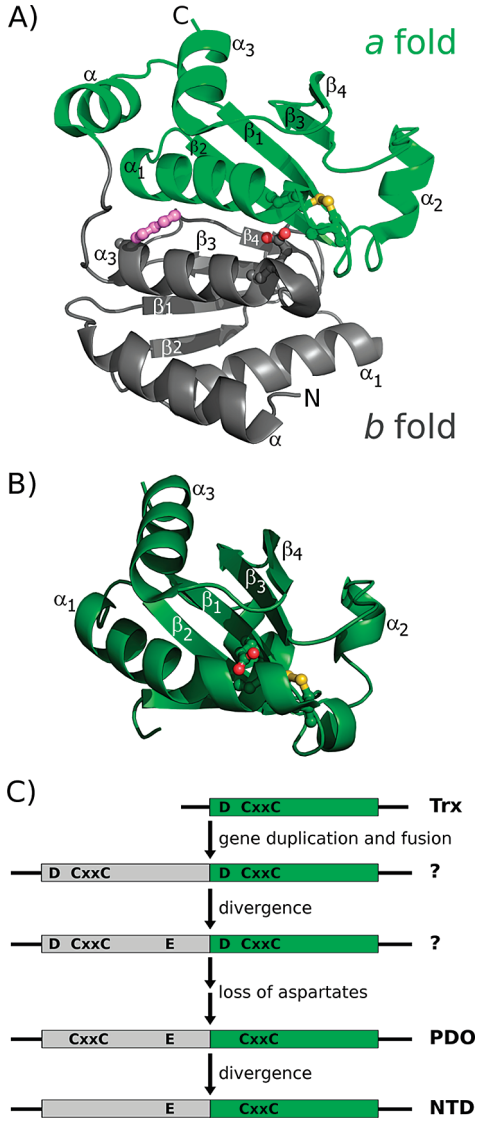

FIGURE 2: Comparison of the NTD and *Ec*Trx. (A) Ribbon diagram of the NTD (PDB entry 1ZYN). The two Trx folds are colored gray (***b*** fold) and green (***a*** fold). The redox active cysteines (Cys129 and Cys132 with sulfur atoms colored yellow), conserved glutamic acid (Glu86 with oxygen atoms colored red), and fluorescence reporter (Trp96 with the side chain colored purple) are shown as ball-and-stick diagrams. Secondary structure elements are labeled; conserved secondary structure elements of the Trx fold are labeled with subscripts. Helix α_2 of the Trx fold is not present in the ***b*** fold of the NTD. The only secondary structure element in the NTD that is not in the conserved Trx fold is an α-helix, labeled α, that is present at the beginning of both the ***a*** and ***b*** folds. The letters N and C mark the N- and C-termini, respectively, of the NTD. (B) Ribbon diagram of *Ec*Trx (PDB entry 2TRX) in the same orientation as the ***a*** fold of the NTD in panel A. The redox active cysteines and conserved aspartic acid are shown as in panel A, and only the conserved structural elements of the Trx fold are labeled. A structure-based sequence alignment of *Ec*Trx on the ***a*** and ***b*** folds of the NTD gives a 1.3 Å (for 73 Cα atoms) and 1.5 Å (for 51 Cα atoms) rmsd with 15 and 16% sequence identity, respectively, while alignment of the two NTD folds gives an rmsd of 1.3 Å (for 46 Cα atoms) with 14% sequence identity. (C) The proposed evolution of the NTD begins with an ancestral Trx-like protein that has an active site aspartic acid and redox active disulfide (D and CxxC in the top green bar). Gene duplication and fusion (*53*) creates a hypothetical ancestral protein that has two folds and two active sites (each containing a buried aspartic acid). Sequence divergence introduces a buried glutamic acid into the ***b*** fold (shown as an E). With the addition of this charged group to the active site, there has been speculation that the oxidoreductase activity of the protein could be rescued after the loss of the buried aspartate in the ***a*** fold (*5*). The active site CxxC motif in the ***b*** fold seen in the evolutionary intermediate, protein disulfide oxidoreductase (PDO), is lost with time. The fold coloring is as in panel A.

BL21*DE3 using N-5052 medium (*14*) containing 2.5 g/L $^{15}NH_4Cl$. ^{15}N- and ^{13}C-labeled NTD was purified from cells grown in M9 minimal medium containing 1 g of $^{15}NH_4Cl$ and 2 g of [^{13}C-U]glucose per liter. After elution on a Superose 12 column, all concentrated samples were further purified on a Superdex 75 column (GE Healthcare) with a running buffer of 50 mM sodium phosphate, 200 mM sodium sulfate, and 1 mM sodium azide (pH 7.3). The purified protein was exchanged into 50 mM potassium phosphate buffer (pH 6.5), with 50 mM potassium chloride. For NTD-$(SH)_2$, a 10-fold excess of DTT was added during buffer exchange. The protein concentration was determined from the absorbance at 280 nm using an extinction coefficient of 15100 M^{-1} cm^{-1} (*6*).

Size-Exclusion Chromatography. NTD-S_2 and NTD-$(SH)_2$ were run on a Superdex 75 HR 10/30 size-exclusion column (flow rate of 0.5 mL/min) as described above with a 5−20 μL injection of a 0.8 mM protein solution. For NTD-$(SH)_2$, 5 mM βME was added to the running buffer. Proteins were detected by the absorbance at 280 nm, refractive index, and multiangle light scattering (miniDawn, Wyatt).

Unfolding Measured by Intrinsic Fluorescence and Circular Dichroism. Urea stock solutions for denaturation unfolding studies were prepared as described previously (*15*) in 50 mM potassium phosphate buffer (pH 6.5) with 50 mM potassium chloride. Intrinsic fluorescence emission spectra of the single tryptophan in the NTD were acquired on a Jobin Yvon/Spex spectrofluorometer. The excitation wavelength was set to 295 nm, and fluorescence emission spectra were scanned from 310 to 380 nm. A sample cell of 0.5 cm and slit widths of 2 and 4 nm or 2 and 2 nm were used for data collection. To limit the impact of photobleaching, only one fluorescence measurement was recorded on each sample. Two sets of samples were prepared with urea concentrations ranging from 0 to 7.8 M in 50 mM potassium phosphate buffer (pH 6.5), with 50 mM potassium chloride: the first containing 2 μM protein [200 μM DTT added for NTD-$(SH)_2$] and the second containing 20 μM protein [2 mM DTT added for NTD-$(SH)_2$]. Blanks were prepared for each data point, and the fluorescence of the blank was subtracted from the fluorescence of the protein sample.

Circular dichroism (CD) experiments were conducted on a Jasco J-720 spectropolarimeter in a 0.1 cm sample cell, and spectra were scanned from 200 to 250 nm. After fluorescence data collection, the same 20 μM protein samples [2 mM DTT added for NTD-$(SH)_2$] were used for CD experiments. Additional samples prepared with 20 μM protein and 200 μM DTT for NTD-$(SH)_2$ were also measured. For all unfolding experiments, samples were equilibrated for 12 h at 4 °C before data collection at 25 °C.

The resulting transition curves were analyzed by nonlinear least-squares curve fitting using a two-state model for unfolding following methods developed by Bolen and Santoro (*16*, *17*) and described by Hall et al. (*18*). Individual and global fits to the data were modeled. Data were normalized to set the population of folded protein at 0 M urea equal to 1.

Attempts to perform thermal unfolding experiments were not successful due to decreased protein solubility at elevated temperatures.

NMR Spectroscopy. NMR spectra were collected on a 600 MHz Bruker DRX spectrometer at 298 K. Samples were prepared with a protein concentration of 1 mM in 50 mM potassium phosphate buffer (pH 6.5), 50 mM potassium chloride, 10% (v/v) D_2O, and 1 mM DSS, maleic acid, sodium azide, and protease inhibitor (Roche). For NTD-$(SH)_2$ samples, 10 mM DTT was added.

$^1H-^{15}N$ HSQC experiments were conducted using Echo/Antiecho-TPPI gradient selection. Backbone assignments of NTD-S_2 were obtained using standard three-dimensional triple-resonance CBCACONH and HNCA experiments conducted with ^{15}N- and ^{13}C-labeled NTD. Backbone resonance assignments for NTD-$(SH)_2$ have previously been determined (*19*). Backbone chemical shift assignments for NTD-S_2 have been deposited in the BioMagResBank as entry 16265.

Backbone ^{15}N Relaxation. Backbone amide relaxation parameters (^{15}N R_1, R_2, and steady-state $^1H-^{15}N$ heteronuclear NOE) were measured using pulse sequences described by Farrow et al. (*20*). The R_1 experiments were conducted with relaxation delay times of 50 (2×), 100 (2×), 250, 500, 1000, 2000, and 3000 ms, and the R_2 relaxation data were acquired using relaxation delays of 20, 35, 48 (2×), 65, 80, and 100 ms. Duplicate measurements (marked with 2×) were used to estimate experimental error. Steady-state heteronuclear NOE experiments were conducted in the presence and absence of amide proton saturation. Spectra with proton saturation utilized a 3 s period of saturation and an additional delay of 1.5 s.

NMR Data Analysis. NMR spectra were processed using NMRPipe (*21*) and analyzed with Burrow Owl (*19*). The change in $^1H-^{15}N$ HSQC chemical shift (ΔN−H) between NTD-S_2 and NTD-$(SH)_2$ was determined using the equation $\Delta N-H = [(\Delta^1H)^2 + (\Delta^{15}N)^2]^{1/2}$ after multiplying the ^1H chemical shift by 6.2 (fractional difference in ^{15}N:^1H spectral widths) to eliminate ^{15}N chemical shift bias (*22*).

For all dynamics experiments, peak intensities were measured as peak height at the highest point and the error associated with peak height measurement was taken to be the baseline noise. R_1 and R_2 values were determined by fitting the measured peak heights versus time plots to the relationship $I = I_0e^{-\text{rate}(t)}$, where t is the relaxation delay, I is the intensity of the peak at time t, and I_0 is the initial peak intensity. Curve fitting was performed using Curvefit (http://cpmcnet.columbia.edu/dept/gsas/biochem/labs/palmer/software/curvefit.html) and visualized using Grace (http://plasma-gate.weizmann.ac.il/Grace/).

Steady-state NOE values were obtained from the ratio of peak intensities in the presence and absence of amide proton saturation. The error associated with the NOE value was calculated from the equation $\sigma/\text{NOE} = [(\sigma I_A/I_A)^2 + (\sigma I_B/I_B)^2]^{1/2}$, where I and σI denote the intensity of the peak and its baseline noise, respectively, and the subscripts A and B denote spectra recorded in the presence and absence of proton saturation, respectively (*23*).

Lipari−Szabo Analysis of Relaxation Data. Backbone amide relaxation parameters were analyzed with the extended Lipari−Szabo formalism (*24*−*27*) using TENSOR2 (*28*) to assess global tumbling and internal motions. The ^{15}N CSA was set to −170 ppm, and an N−H bond length of 1.02 Å was used. For each data set, a global tumbling correlation time (τ_c) was calculated from the residues assumed to have a negligible exchange contribution to ^{15}N relaxation determined using the method described by Tjandra et al. (*29*) and verified using the more stringent method described by Pawley et al. (*30*).

Internal motions were determined using Monte Carlo sampling methods and *F*-test validation incorporated in TENSOR2 (*28*). Five standard models were used to describe internal mobility with motion complexity increasing with model number (*24*, *27*). A model for the internal motions was rejected if

the experimental χ^2 value was higher than the simulated χ^2 value at the 90% confidence limit. Residues that were not adequately fit by any of the five models for motion were omitted from further analysis. For anisotropic analyses, PDB entries 1ZYP and 1ZYN were used for NTD-$(SH)_2$ and NTD-S_2, respectively (*13*).

Hydrogen−Deuterium Exchange. Samples were prepared for NMR as described above but with a buffer pH of 6.2, flash-frozen, and lyophilized. Hydrogen−deuterium (H−D) exchange was initiated by dissolving the lyophilized sample in 100% ^2H_2O. The pH of the samples was verified to be 6.2 both before and after the experiment. The dead time of the experiment, defined as time between the first exposure to ^2H_2O and the middle of the first HSQC experiment, was 27 min for NTD-S_2 and 33 min for NTD-$(SH)_2$. $^1H-^{15}N$ HSQC spectra were collected continuously for the first 18 h. Data were collected on the NTD-S_2 sample for only an additional 4 days due to protein precipitation. Data collection continued on the NTD-$(SH)_2$ sample once every 2 days for 26 days to monitor the disappearance of peaks. No precipitation was observed for the NTD-$(SH)_2$ sample during this interval. The H−D exchange rates were determined using the equation $I = I_0 e^{-\text{rate}(t)} + \Omega$, where t is the exchange time, I is the intensity of the peak at time t, I_0 is the initial peak intensity, and Ω is the extrapolated offset value from zero intensity caused by residual hydrogen present in the sample. Curve fitting was done as previously described for R_1 and R_2 relaxation rate determination. Exchange rates were estimated for residues where peak intensity loss could not be fit to an exponential decay. A minimum exchange rate for peaks not detected at the first data point was estimated assuming $I/I_0 = 0.1$, and a maximum exchange rate for peaks present at the last time point of the reduced data set (and unable to be exponentially fit) was estimated assuming $I/I_0 = 0.9$. Protection factors were determined using Sphere (*31*, *32*). The estimated stability of the protein based on H−D exchange rates was calculated using

$$\Delta G^\circ_{HX} = -RT \ln(k_{ex}/k_{int}) \quad (1)$$

where ΔG°_{HX} is the free energy of unfolding and k_{ex} and k_{int} are the observed (estimated) and intrinsic exchange rates, respectively, for the slowest exchanging residues (*33*).

Molecular graphics were created using pymol (*34*), and figures were prepared using Gimp.

RESULTS

Size-Exclusion Chromatography. Size-exclusion chromatography confirms that at the concentrations used NMR, for both NTD-$(SH)_2$ and NTD-S_2 are monomeric with similar molecular shapes (Figure 1 of the Supporting Information). The molecular mass determined from multiangle light scattering is 22620 ± 450 Da, consistent with the calculated mass for a monomeric protein of 22292 Da.

Chemical Shift Comparison for NTD-$(SH)_2$ and NTD-S_2. Backbone amide resonance assignments for NTD-$(SH)_2$ were completed for 191 of the 192 non-proline residues (*19*). Here, the equivalent assignments for NTD-S_2 were completed for 188 residues; resonances were missing for residues 28, 85, and 134 and were weaker for residues 128 and 129. Comparison of the ^{15}N and ^1H chemical shifts between NTD-$(SH)_2$ and NTD-S_2 shows that the residues with the largest changes cluster around the active site; chemical shift differences of >0.1 ppm occur for residues 86−89, 124−129, 136, 137, 171−173, 184, and 185 (Figure 2 of the Supporting Information). Residues with signal loss in NTD-S_2 are also localized near the active site, suggesting their intensity loss reflects changes in active site dynamics due to exchange broadening.

Unfolding Studies. Protein stabilities were determined by monitoring changes in both fluorescence emission and CD signal with an increase in urea concentration. The NTD's single tryptophan residue, Trp96, is partly buried at the interface of the two Trx folds (Figure 2A); atoms Nε1, Cζ2, and Cη2 are ∼50% accessible (*35*). Consistent with the partial solvent exposure of Trp96, its fluorescence maximum occurs at 347 nm in the folded state (compared to ∼327 nm for a fully buried tryptophan) and shifts to 357 nm in the unfolded protein. The initial fluorescence intensity is the same for NTD-$(SH)_2$ and NTD-S_2, consistent with earlier results (*36*).

Urea-induced denaturation at pH 6.5 yields similar profiles for NTD-$(SH)_2$ and NTD-S_2 with an apparent single-step transition irrespective of the spectral probe used to follow unfolding (Figure 3). Each of the four curves was individually fit to a two-state unfolding model. The extrapolated $\Delta G^\circ_{H_2O}$ value for NTD-$(SH)_2$ unfolding is 6.5 kcal/mol as measured by either CD or fluorescence. Similarly, the extrapolated $\Delta G^\circ_{H_2O}$ value for NTD-S_2 unfolding is 6.6 kcal/mol as measured by either technique. Despite the equivalence of $\Delta G^\circ_{H_2O}$ values determined from the unfolding transition monitored by the two techniques, the curves are clearly not superimposable, and the calculated urea concentration for the midpoint of unfolding is 0.3 M higher when measured by CD (Table 1). This difference necessitates a closer examination of the two-state unfolding assumption.

In the standard two-state model of protein unfolding, a global (i.e., simultaneous) fit of both fluorescence and CD data should give parameters that fit well to both of the individual curves (*37*). Simultaneous fits of the transition curves of NTD-$(SH)_2$ and NTD-S_2 give midpoints of unfolding of 3.9 and 4.1 M urea. The respective extrapolated $\Delta G^\circ_{H_2O}$ values for unfolding are 6.5 and 6.6 kcal/mol. The globally determined parameters fit the data well (Figure 3 and Table 1). As no apparent intermediate was detected in the unfolding data, a three-state unfolding model was not pursued.

Unfolding of the NTD-$(SH)_2$ in the presence of 10- and 100-fold excesses of DTT (0.2 and 2 mM DTT, respectively) gave similar results when monitored by CD (data not shown).

^{15}N Backbone Relaxation Dynamics. Backbone relaxation dynamics were measured with R_1, R_2, and steady-state heteronuclear NOEs for 149 and 146 residues in NTD-$(SH)_2$ and NTD-S_2, respectively. Excluded residues correspond to overlapping peaks or to those that are too weak for accurate measurements. The relaxation rates along the backbone of NTD-$(SH)_2$ and NTD-S_2 show similar trends, including a disordering of

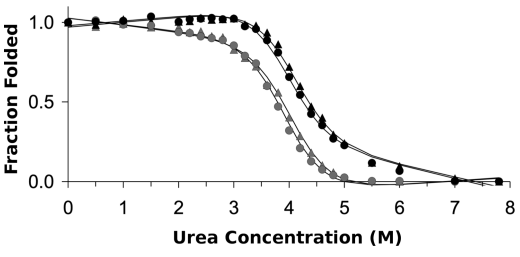

FIGURE 3: Global, cooperative denaturation of the NTD by urea. The reversible unfolding of NTD-S_2 (triangles) and NTD-$(SH)_2$ (circles) in urea was followed by fluorescence (gray symbols) and CD (black symbols). Solid curves are global fits of the unfolding data to a two-state unfolding model.

the C-terminus (Figure 3 of the Supporting Information). Overall, NTD-$(SH)_2$ and NTD-S_2 have comparable R_1 and NOE values, but NTD-S_2 has notably higher R_2 values (Figure 4 and Table 2).

Model free analysis of backbone relaxation data was carried out using the axially symmetric anisotropic diffusion model. Global tumbling correlation times of 13.08 ± 0.01 and 13.63 ± 0.01 ns were calculated for NTD-$(SH)_2$ and NTD-S_2, respectively, using the filter described by Tjandra et al. (*29*). For internal motions (Figure 4 of the Supporting Information), the majority of residues were fit by models 1 and 3 in NTD-$(SH)_2$ and model 4 in NTD-S_2. Despite the differences in model type, the S^2 terms are similar across the backbone for both redox states (Figure 4 and Table 2) with an average of 0.89 ± 0.01 for NTD-$(SH)_2$ and 0.94 ± 0.02 for NTD-S_2 which indicate that overall, both redox states are well ordered on the fast time scale. In contrast, a clear difference is seen in the R_{ex} values, with NTD-S_2 having both more residues modeled with R_{ex} terms (79 vs 48) and a higher average value (3.7 ± 0.5 vs 2.2 ± 0.4) (Figure 4 and Table 2). As R_{ex} terms measure intermediate chemical exchange, these data suggest more intermediate time scale conformational heterogeneity in NTD-S_2. To verify that the R_{ex} terms described by the model free analysis, especially those for the NTD-S_2, were not due to incorrect global tumbling correlation times, the two-part filter described by Pawley et al. (*30*) was used determine a more accurate description of the tumbling of the protein. With this method, global correlation times of 13.47 ± 0.01 and 14.35 ± 0.03 ns were determined for NTD-$(SH)_2$ and NTD-S_2, respectively. The internal motions determined from the model free analysis using these more stringently determined τ_c values slightly altered the qualitative results for both NTD-$(SH)_2$ and NTD-S_2 but led to no quantitative changes (data not shown).

H−D Exchange Monitored by NMR. The EX2 exchange limit (*38*) was determined to be the more likely mechanism for hydrogen exchange in the NTD; plots of k_{ex} versus k_{int} for secondary structure elements in the ***a*** and ***b*** folds for both NTD-S_2 and NTD-$(SH)_2$ give straight lines with slopes ranging from 0.8 to 1.1 (data not shown). This is close to the expected slope of 1 for an EX2 exchange mechanism (*39*, *40*). Protection factors were calculated at pH 6.2 and 25 °C for the fast, intermediate, and slowest exchanging residues for both NTD-$(SH)_2$ and NTD-S_2 (Figure 5 and Table 1 of the Supporting Information). Fast exchanging residues are defined as those fully exchanged at the first time point (~30 min) for which a minimum exchange rate of $\sim 1 \times 10^{-3}$ s^{-1} is estimated. The fast exchanging residues are located primarily on the surface of the protein.

For intermediate exchanging residues, rate constants determined by fits of a single exponential to decreasing peak intensity with time range from 1×10^{-3} to 3×10^{-7} s^{-1}. Comparison of

Table 1: Thermodynamic Parameters for Urea-Induced Unfolding

	$\Delta G°_{H_2O}$ (kcal/mol)	*m* (kcal/mol/M)	unfolding midpoint (M)
NTD-S_2			
CD (220 nm)[a]	6.6	1.6	4.2
fluorescence[b]	6.6	1.7	3.9
global[c]	6.6	1.6	4.1
NTD-$(SH)_2$			
CD (220 nm)[a]	6.5	1.6	4.1
fluorescence[b]	6.5	1.7	3.8
global[c]	6.5	1.7	3.9

[a] Parameters determined by fitting unfolding data obtained from the CD signal at 220 nm. [b] Parameters determined by fitting unfolding data obtained from fluorescence intensity at 347 nm. [c] Parameters determined by simultenously fitting unfolding data obtained from CD and fluorescence.

Table 2: Overall ^{15}N Backbone Dynamics Summary

	NTD-S_2	NTD-$(SH)_2$
R_1 (s^{-1})	1.09 ± 0.02	1.04 ± 0.01
R_2 (s^{-1})	20.8 ± 0.4	17.3 ± 0.3
NOE	0.76 ± 0.06	0.79 ± 0.03
τ_c (ns)	13.63 ± 0.03	13.08 ± 0.01
S^2	0.94 ± 0.02	0.89 ± 0.01
R_{ex} (s^{-1})	3.7 ± 0.5	2.2 ± 0.4

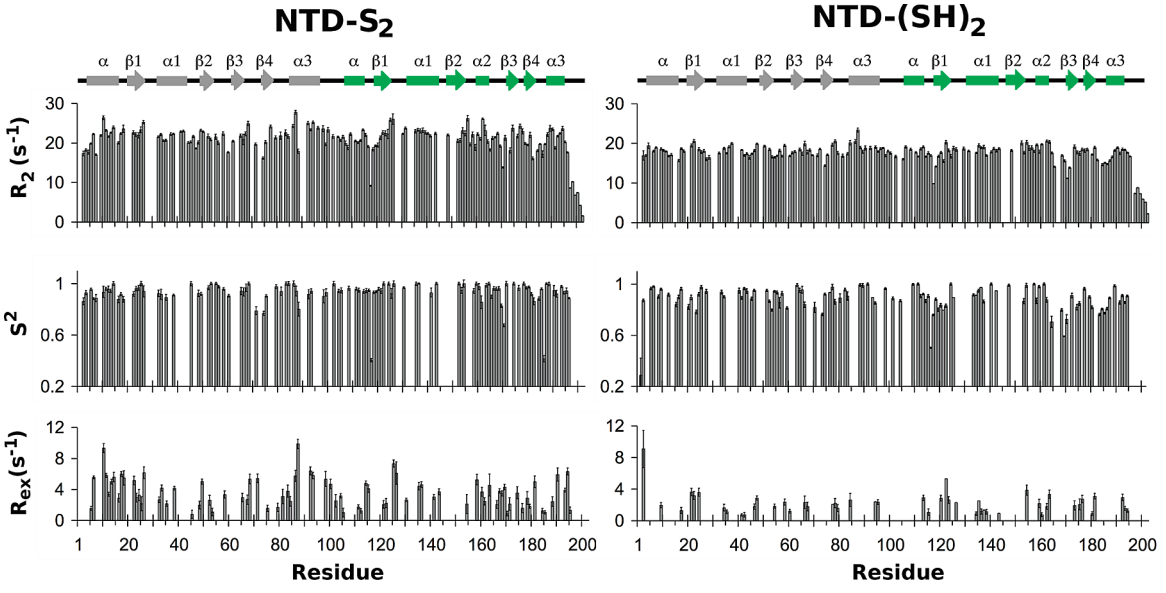

FIGURE 4: Select data from ^{15}N backbone relaxation experiments and model free analyses. Shown are R_2, S^2, and R_{ex} data for NTD-S_2 (left) and NTD-$(SH)_2$ (right) plotted per residue. Secondary structure elements with labels shown above the plots are colored by fold as in Figure 2A. Additional relaxation data are given as Supporting Information.

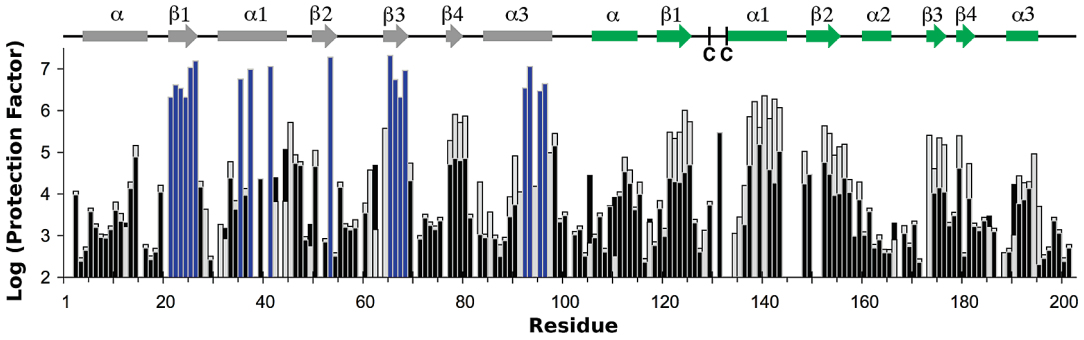

FIGURE 5: H−D exchange protection factors for NTD-S_2 are lower than for NTD-$(SH)_2$. Overlay of protection factors for NTD-S_2 (black bars) and NTD-$(SH)_2$ (gray bars). Residues for which there is no bar or only one bar (all gray or all black) are those amides that were not measured due to overlap or unassigned peaks. Blue bars are shown for the estimated protection factors of the slowest exchanging residues (21−26, 35, 37, 41, 53, 65−68, 92, 93, 95, and 96). For residues where a protection factor was measured in both redox states, a gray bar and a black bar are overlaid and the color on top indicates which form is more protected (more slowly exchanging). Residues 77−80, 83, 90, 121−125, 136, 137, 141−143, 148, 152−156, 174−176, 179−181, and 191 are 5−100-fold more protected in NTD-$(SH)_2$, while only residues 42, 44, 110, and 190 are more protected in NTD-S_2. The residues that are significantly faster exchanging in NTD-S_2 (shorter bars) cluster in α1, β1, β2, β3, and β4 of the ***a*** fold and in β4 and near Glu86 of the ***b*** fold. Secondary structure elements are shown with labels above the plot and are colored by fold as in Figure 2A. The positions of active site Cys129 and Cys132 are indicated. Protection factors are computed for exchange rate constants determined at pH 6.2 and 25 °C.

protection factors for intermediate exchanging amides reveals that many residues distributed throughout the sequence are ~10-fold more slowly exchanging (more protected) in NTD-$(SH)_2$. These residues cluster in β1, α1, β2, β3, and β4 of the ***a*** fold and in β4 of the ***b*** fold. Only four amides are > 5-fold more protected in NTD-S_2 (residues 42, 44, 110, and 190); these are located on the protein surface distant from the active site.

The slowest exchanging residues, those with less than 10% intensity loss over the course of the experiment (~27 days), were given an estimated upper limit exchange rate constant of 6×10^{-8} s^{-1}. Although the data sets used for NTD-$(SH)_2$ and NTD-S_2 were collected for different lengths of time, both identify the same group of slowest exchanging residues; all are associated with secondary structure elements β1, α1, β2, β3, and α3 of the ***b*** fold. On the basis of the maximal estimated protection factors for NTD-$(SH)_2$, its apparent stability by hydrogen exchange criteria ($\Delta G°_{HX}$) is ~10 kcal/mol.

DISCUSSION

Oxidation Does Not Significantly Change the Global Stability of the NTD. The combined use of CD and fluorescence quenching monitors both secondary and tertiary structural changes that occur with an increase in the level of denaturant. While the fluorescence and CD unfolding profiles are not completely overlapping, the finding that global (simultaneous) fits to the urea unfolding data for NTD-$(SH)_2$ and NTD-S_2 give parameters that agree with those obtained from fits to individual curves (Table 1) and fit both curves well (Figure 3) supports a cooperative two-state unfolding model (*37*). Very similar $\Delta G°_{H_2O}$ values of 6.5 and 6.6 kcal/mol are obtained for NTD-$(SH)_2$ and NTD-S_2, respectively. The apparent two-state unfolding behavior is consistent with the absence of detectable stable intermediates and suggests that the two folds of the NTD do not significantly separate before the protein unfolds.

The apparent stability obtained by H−D exchange analysis is higher (~10 kcal/mol) than that determined by fluorescence and CD unfolding studies, probably due to residual structure in the unfolded state (*41*, *42*); however, both results indicate that the NTD is quite stable. The extrapolated $\Delta(\Delta G°_{H_2O})$ value between NTD-$(SH)_2$ and NTD-S_2 of 0.1 kcal/mol derived from urea denaturation (Table 1) is our best measure of the increased stability of NTD-S_2. This difference is considerably lower than the 1.2 kcal/mol net stabilization expected solely from disulfide bond oxidation decreasing the conformational freedom of the unfolded state by closing a loop four residues in length (*43*). The difference between expected and observed values implies that upon disulfide oxidation, other factors collectively decrease $\Delta(\Delta G°_{H_2O})$.

Oxidation Increases the Conformational Heterogeneity of the NTD. To probe the effect of cysteine oxidation and reduction on the structure and dynamics of residues around the active site and the protein as a whole, we compare chemical shifts, peak broadening, relaxation parameters, and hydrogen exchange rates between the two redox forms. $^1H-^{15}N$ HSQC spectra of NTD-$(SH)_2$ and NTD-S_2 show chemical shift changes primarily localized to residues near the active site, and along the active site ends of helices α1 of the ***a*** fold and α3 of the ***b*** fold (Figure 2 of the Supporting Information). These data suggest that while the overall structure is similar in the two redox forms, there are local structural changes in the active site that may be propagated down the helices containing active site residues. In addition to peak shifts, apparent chemical exchange broadening for active site residues Ser128 and Cys129 and nearby residues in the NTD-S_2 spectrum indicates conformational heterogeneity on the millisecond microsecond time scale that is absent in NTD-$(SH)_2$. This qualitative measurement of the differences between NTD-$(SH)_2$ and NTD-S_2 supports the more quantitative model free analyses of internal motions which show that intermediate time scale motions differ significantly in the two redox forms; NTD-S_2 has substantially more residues with motions reflected in a higher R_{ex} term (Figures 4 and 6).

Dynamics differences between NTD-$(SH)_2$ and NTD-S_2 are strongly evident from H−D exchange results which indicate that amides in NTD-S_2 are faster exchanging (Figure 5, orange and red colors in Figure 7A). The consistent pattern is an ~10-fold (1 log unit) decrease in protection factor for five elements of secondary structure in the catalytic ***a*** fold and one in the ***b*** fold (β4 at the interface of the two folds). It is noteworthy that NTD-S_2 shows decreased protection despite being slightly more stable. This implies that the higher exchange rates for intermediate exchanging residues in NTD-S_2 do not arise from exchange processes involving global unfolding, but rather from increased internal fluctuations within the folded-state ensemble of NTD-S_2 (Figure 8).

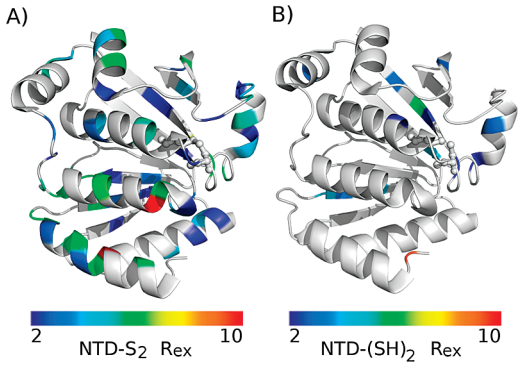

FIGURE 6: Different intermediate exchange motions for NTD-S_2 and NTD-$(SH)_2$. Model free analysis results for intermediate time scale motions [R_{ex} (Figure 4, bottom graphs)] are plotted on the crystal structure. Comparison of (A) NTD-S_2 and (B) NTD-$(SH)_2$ reveals an increase in R_{ex} motions across the entire protein for NTD-S_2 (green, yellow, and red). The same coloring scale is used for both panels, and the redox active disulfide is shown as a ball-and-stick diagram in both structures. Residues with R_{ex} values of $< 2\ s^{-1}$ or with no measurements are colored gray.

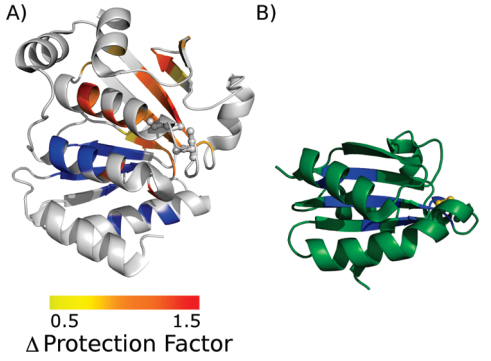

FIGURE 7: Two Trx folds of the NTD display different levels of protection from exchange. (A) Data shown in Figure 5 are mapped on the crystal structure. The slowest exchanging residues (blue) are located in the ***b*** fold, while residues with significant differences in protection factor with oxidation (colored yellow to red by the magnitude of difference) are located around the active site and found primarily in the ***a*** fold. The redox active disulfide is shown as a ball-and-stick diagram, and residues with no measurements or with a difference of < 0.5 in protection factor are colored gray. (B) The slow exchanging residues (blue) of *Ec*Trx are located in the core of the Trx fold (data from ref (*51*)). The redox active disulfide is shown as a ball-and-stick diagram with sulfur atoms colored yellow. *Ec*Trx is aligned with the ***b*** fold of the NTD.

What are the possible origins of the increased motions in NTD-S_2? Although chemical exchange broadening, larger R_{ex} values, and faster H−D exchange rates indicate increased internal fluctuations in NTD-S_2, the motions responsible for the increases are not necessarily the same. This is apparent as increased values of R_{ex} are observed throughout the ***a*** and ***b*** folds of NTD-S_2 and report motions on the millisecond to microsecond time scale. However, increased H−D exchange rates are observed primarily for residues in the ***a*** fold and some residues near Glu86 in the ***b*** fold. These motions reported by folded-state H−D exchange of amide N−H groups, which in the crystal structure are buried and intramolecularly H-bonded, cannot at present be attributed to any specific time scale (*42*). The fact that buried amides exchange by a folded-state mechanism means that the folded protein moves in ways that permit access of buried NH groups to water. The pattern of increased exchange rates in the ***a*** fold of NTD-S_2 (Figure 7A) suggests

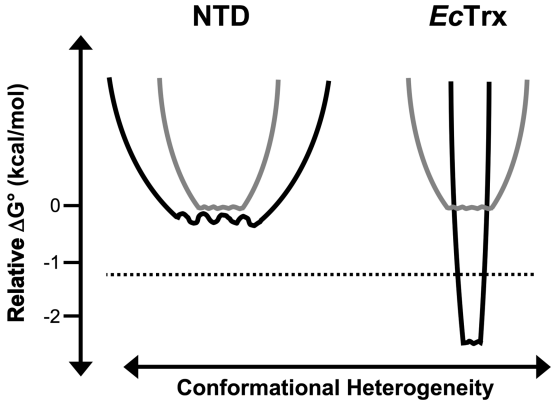

FIGURE 8: Inferred energy landscapes for the NTD and *Ec*Trx. Schematic energy wells illustrate changes in energy landscapes that accompany oxidation: the width of the wells represents qualitative conformational heterogeneity as inferred from H−D exchange behavior, and the roughness at the bottom of the wells represents qualitative intermediate time scale motions as inferred from R_{ex} (see the text). The reduced states of the NTD and *Ec*Trx (gray wells) are shown with the same energy landscape that has the bottom of the well arbitrarily set to zero. The oxidized states (black wells) are drawn to represent the inferred quantitative changes in thermodynamics relative to the reduced state. The dotted line marks the expected 1.2 kcal/mol stability increase for the oxidized form due to the formation of the disulfide bond (*43*). Oxidation of the NTD slightly increases stability and causes increased internal fluctuations (wider well) of rapidly interconverting states on an intermediate time scale (rougher well). Oxidation of *Ec*Trx increases stability (*49*) and decreases the conformational heterogeneity (*51*, *52*) (narrower well) without large changes in intermediate time scale motions (*50*) (similar roughness).

movement of helix α1 relative to the β-sheet against which it is packed. Collective motion of the entire helix α1 as in local unfolding or unraveling is unlikely as an inside/outside pattern of slow and fast exchange rates is observed. The data are consistent with changes in numerous, local, and small-scale motions in α1 and in strands β1, β2, β3, and β4 of the ***a*** fold (red and yellow in Figure 7A). In any case, there is little or no change in average secondary structure as indicated by similar CD spectra for NTD-S_2 and NTD-$(SH)_2$ (data not shown) and published crystal structures (*13*).

The Two Trx Folds Have Distinct Dynamics Not Detected in Crystal Structures. Protein crystal structures provide both a three-dimensional image and an estimate of time-averaged atomic mobility reported as the *B*-factor (temperature factor). For the NTD, crystal structures show no significant conformational or mobility differences between NTD-$(SH)_2$ and NTD-S_2 as is expected on the basis of Trx and Trx-like domains in other proteins (*44*). Also, as measured by *B*-factors, the ***a*** and ***b*** folds have remarkably similar apparent mobility along the chain (Figure 9). In both folds, helix α is highly mobile, and in the rest of the fold, core regions with *B*-factors near 20−25 $Å^2$ alternate with loop regions having higher *B*-factors.

In contrast, H−D exchange data convincingly show that the dynamic and thermodynamic behaviors of the ***a*** and ***b*** folds are quite distinct. Typically, the final group of amides to exchange in a protein identifies the packed secondary structure that constitutes the core of the protein as these regions are accessible to exchange only when the protein undergoes global unfolding (*45*). For the NTD, these are all in the ***b*** fold (blue in Figure 7A). In contrast, corresponding secondary structure elements in the ***a*** fold are 10−100-fold faster exchanging in NTD-$(SH)_2$ and 100−1000-fold faster exchanging in NTD-S_2 (Figure 5). Relative to

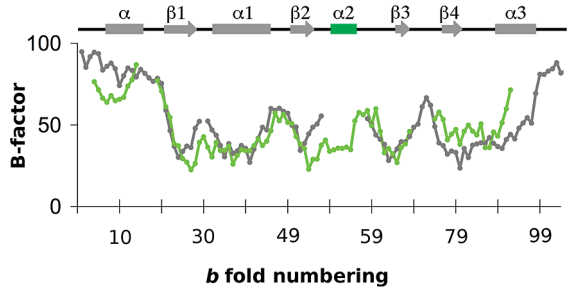

FIGURE 9: ***a*** and ***b*** folds show similar mobility in crystal structures. The *B*-factors along the chain from NTD-S_2 (PDB entry 1ZYN) for the ***a*** fold (green) and ***b*** fold (gray) are mapped onto the ***b*** fold by a structure-based sequence alignment. Secondary structure elements are indicated: helix α2 is present only in the ***a*** fold and is colored green. Other NTD crystal forms (PDB entries 1ZYP and 1HYU) behave similarly, suggesting that crystal packing in not a major influence. Minor local differences in *B*-factor between the two folds occur in regions where structural elements have different solvent accessibilities due to the fold−fold packing.

that in the ***b*** fold, this substantially more rapid exchange in the ***a*** fold, even in the most protected residues, implies a much greater folded-state mobility in the ***a*** fold. The dramatic differences between the folds and striking redox sensitive internal fluctuations (discussed above) are likely to be related to the biological role of the NTD in the redox cascade (Figure 1). This is supported by the observations that (1) upon oxidation, the largest changes in both R_{ex} and H−D exchange are clustered around the active site and in the catalytic ***a*** fold and (2) in the ***b*** fold, strand β4 (which packs under the active site), and residues in the vicinity of Glu86, exchange faster in NTD-S_2, along with others in the ***a*** fold.

The clear divergence of a Trx fold that has very low mobility independent of redox state (the ***b*** fold) from a Trx fold that displays redox-dependent dynamics (the ***a*** fold) suggests that the functions of the two folds have become specialized. The ***b*** fold not only contributes key residues to the active site (Glu86) but also provides the core stability of the protein. This might allow the ***a*** fold, which contains most of the active site structure, to acquire dynamic properties which enhance catalysis.

*Similarities and Differences between the NTD and Ec*Trx. The overall structure of *E. coli* Trx (*Ec*Trx) determined by NMR (*46*) or crystallography (*47*, *48*) is very similar for the two redox forms with only small conformational changes observed for active site residues. This is consistent with our data for the NTD. Interestingly, there is a significantly larger difference in stability between oxidized and reduced *Ec*Trx (2.4 kcal/mol) (*49*) compared to the NTD (0.1 kcal/mol).

^{15}N backbone relaxation analyses of *Ec*Trx (*50*) show that the overall fast motions (S^2 values) are very similar in both redox states, with three loops (before β1, α2−β3, and β4−α3) being particularly dynamic on this time scale and the latter two important to catalysis. In the NTD, there are similar low S^2 values for the α2−β3 loop (and to a lesser extent for the β4−α3 loop) in the ***a*** fold, but no hint of such dynamics are present in the ***b*** fold. The conservation of these fast motions in loops that pack on the NTD active site disulfide and not in the equivalent loops of the ***b*** fold is consistent with their importance in catalysis.

The slow exchanging core in *Ec*Trx (*51*, *52*) contains residues mostly from β1, β2, and β3 (Figure 7B). In the NTD, the slowest exchanging residues which include the slow exchanging core are only present in the ***b*** fold and are located in strands β1, β2, and β3 as well as helices α1 and α3 (Figures 5 and 7A). The ***a*** fold shows similar relative features (β-strands being local maxima of protection); however, the absolute protection levels are much lower, and all amides in the ***a*** fold exchange from the folded state with no contribution from global stability.

The most dramatic differences between *Ec*Trx and the NTD are redox-associated changes in dynamics. In *Ec*Trx, oxidation does not cause a change in fast motions but decreases the level of conformational exchange for a few active site residues (between α2 and β3) (*50*) and increases protection from H−/D exchange specifically for those residues at the active site (*51*). In stark contrast, oxidation of the NTD is associated with widespread increased conformational exchange across the backbone (Figures 4 and 6) and decreased protection from H−D exchange across the ***a*** fold (Figures 5 and 7A). A schematic summary of the changes in protein thermodynamics with oxidation is given in Figure 8.

Evolutionary Divergence of the Two Trx Folds. The opposite trends with oxidation observed for *Ec*Trx and the NTD fit the idea of evolutionary divergence and specialization of the two Trx folds. Folding thermodynamics and H−D exchange show that the NTD is not comprised of two independent Trx folds, each retaining the original functional and dynamic properties of Trx. Instead, we see evidence of an evolved merging of two Trx folds into a single cooperative folding unit along with specialization of function of each Trx fold to produce unique redox functions of a new protein. The ***b*** fold (all but β4 and the residues around Glu86 in α3) provides a largely redox insensitive stable core, and the ***a*** fold (together with β4 from the ***b*** fold) provides the biological redox activity with dynamic behavior coupled to redox state.

The proposed evolutionary origins for the NTD purport a gene duplication and fusion (*53*) that took place in hyperthermophilic archaea (*12*) (Figure 2C). In this context, the covalent linking of the two Trx-like folds could provide a selective advantage as oligomerization is one strategy for the stabilization of hyperthermophilic proteins (*54*−*56*). We propose that initially, each Trx fold had its own stable core and redox activity. Then, with one "superfluous" active site, what would become the ***b*** fold diverged to gain stability and lose activity. Subsequent divergence led to further differentiation of the functional roles of the two folds with strand β4 of the ***b*** fold becoming a functional part of the ***a*** fold. In the evolutionary intermediate PDO, the functions of the two folds already differ, although both folds contain a CxxC motif: only the C-terminal CxxC motif (corresponding to the ***a*** fold of the NTD) is required for oxidoreductase activity, and the N-terminal CxxC motif contributes to isomerase activity (*11*). Following this scenario further, after horizontal gene transfer to bacteria, the two folds were no longer needed for increased stability in a hyperthermic environment, but the requirement for catalysis of Glu86 from the ***b*** fold necessitated its continued conservation in the NTD. Thus, divergence continued with the ***b*** fold losing the CxxC motif and all catalytic function. Interestingly, this result of a partial physical separation of stability and catalysis may provide a distinct advantage of permitting the protein to evolutionarily explore dynamic properties that enhance catalysis beyond what would be achieved in a single fold.

Additionally, as hyperthermophilic proteins are less dynamic at the lower temperatures supporting growth of mesophilic organisms (*57*), the separation of stability and dynamics may be a remnant of a hyperthermophilic adaptation; while the ***b*** fold still reflects the lower internal mobility at mesophilic temperatures, the ***a*** fold has evolved to be more dynamic at these lower

temperatures. It remains to be seen how the dynamic properties of the ***a*** fold impact NTD function, but one intriguing possibility is that the high level of order of NTD-$(SH)_2$ is related to its high specificity for reducing AhpC while the flexibility associated with reduced *Ec*Trx is important for its broad specificity as a protein reductant.

ACKNOWLEDGMENT

We thank Clare Woodward and Justin Hall for helpful discussion, Greg Benison for assistance with NMR data collection and processing, and Mike Hare for help with data fitting.

SUPPORTING INFORMATION AVAILABLE

H−D exchange rates and protection factors, size-exclusion chromatograms, $^{1}H-^{15}N$ HSQC spectra, ^{15}N backbone relaxation data, and model free analysis results. This material is available free of charge via the Internet at http://pubs.acs.org.

REFERENCES

(1) Jacobson, F. S., Morgan, R. W., Christman, M. F., and Ames, B. N. (1989) An alkyl hydroperoxide reductase from *Salmonella typhimurium* involved in the defense of DNA against oxidative damage. Purification and properties. *J. Biol. Chem. 264*, 1488–1496.

(2) Niimura, Y., Poole, L. B., and Massey, V. (1995) *Amphibacillus xylanus* NADH oxidase and *Salmonella typhimurium* alkyl-hydroperoxide reductase flavoprotein components show extremely high scavenging activity for both alkyl hydroperoxide and hydrogen peroxide in the presence of *S. typhimurium* alkyl-hydroperoxide reductase 22-kDa protein component. *J. Biol. Chem. 270*, 25645–25650.

(3) Poole, L. B., and Ellis, H. R. (1996) Flavin-dependent alkyl hydroperoxide reductase from *Salmonella typhimurium*. 1. Purification and enzymatic activities of overexpressed AhpF and AhpC proteins. *Biochemistry 35*, 56–64.

(4) Poole, L. B. (2005) Bacterial defenses against oxidants: Mechanistic features of cysteine-based peroxidases and their flavoprotein reductases. *Arch. Biochem. Biophys. 433*, 240–254.

(5) Wood, Z. A., Poole, L. B., and Karplus, P. A. (2001) Structure of intact AhpF reveals a mirrored thioredoxin-like active site and implies large domain rotations during catalysis. *Biochemistry 40*, 3900–3911.

(6) Poole, L. B., Reynolds, C. M., Wood, Z. A., Karplus, P. A., Ellis, H. R., and Li Calzi, M. (2000) AhpF and other NADH:peroxiredoxin oxidoreductases, homologues of low Mr thioredoxin reductase. *Eur. J. Biochem. 267*, 6126–6133.

(7) Poole, L. B., Godzik, A., Nayeem, A., and Schmitt, J. D. (2000) AhpF can be dissected into two functional units: Tandem repeats of two thioredoxin-like folds in the N-terminus mediate electron transfer from the thioredoxin reductase-like C-terminus to AhpC. *Biochemistry 39*, 6602–6615.

(8) Reynolds, C. M., and Poole, L. B. (2000) Attachment of the N-terminal domain of *Salmonella typhimurium* AhpF to *Escherichia coli* thioredoxin reductase confers AhpC reductase activity but does not affect thioredoxin reductase activity. *Biochemistry 39*, 8859–8869.

(9) Edman, J. C., Ellis, L., Blacher, R. W., Roth, R. A., and Rutter, W. J. (1985) Sequence of protein disulphide isomerase and implications of its relationship to thioredoxin. *Nature 317*, 267–270.

(10) Haugstetter, J., Maurer, M. A., Blicher, T., Pagac, M., Wider, G., and Ellgaard, L. (2007) Structure-function analysis of the endoplasmic reticulum oxidoreductase TMX3 reveals interdomain stabilization of the N-terminal redox-active domain. *J. Biol. Chem. 282*, 33859–33867.

(11) Pedone, E., Ren, B., Ladenstein, R., Rossi, M., and Bartolucci, S. (2004) Functional properties of the protein disulfide oxidoreductase from the archaeon *Pyrococcus furiosus*: A member of a novel protein family related to protein disulfide-isomerase. *Eur. J. Biochem. 271*, 3437–3448.

(12) Becerra, A., Delaye, L., Lazcano, A., and Orgel, L. E. (2007) Protein disulfide oxidoreductases and the evolution of thermophily: Was the last common ancestor a heat-loving microbe? *J. Mol. Evol. 65*, 296–303.

(13) Roberts, B. R., Wood, Z. A., Jonsson, T. J., Poole, L. B., and Karplus, P. A. (2005) Oxidized and synchrotron cleaved structures of the disulfide redox center in the N-terminal domain of *Salmonella typhimurium* AhpF. *Protein Sci. 14*, 2414–2420.

(14) Studier, F. W. (2005) Protein production by auto-induction in high density shaking cultures. *Protein Expression Purif. 41*, 207–234.

(15) Pace, C. N., and Scholtz, J. M. (1997) Protein Structure: A Practical Approach, Oxford University Press, Oxford, U.K.

(16) Bolen, D. W., and Santoro, M. M. (1988) Unfolding free energy changes determined by the linear extrapolation method. 2. Incorporation of ΔG°_{N-U} values in a thermodynamic cycle. *Biochemistry 27*, 8069–8074.

(17) Santoro, M. M., and Bolen, D. W. (1988) Unfolding free energy changes determined by the linear extrapolation method. 1. Unfolding of phenylmethanesulfonyl α-chymotrypsin using different denaturants. *Biochemistry 27*, 8063–8068.

(18) Hall, J., Hall, A., Pursifull, N., and Barbar, E. (2008) Differences in dynamic structure of LC8 monomer, dimer, and dimer-peptide complexes. *Biochemistry 47*, 11940–11952.

(19) Benison, G., Berkholz, D. S., and Barbar, E. (2007) Protein assignments without peak lists using higher-order spectra. *J. Magn. Reson. 189*, 173–181.

(20) Farrow, N. A., Zhang, O., Forman-Kay, J. D., and Kay, L. E. (1994) A heteronuclear correlation experiment for simultaneous determination of ^{15}N longitudinal decay and chemical exchange rates of systems in slow equilibrium. *J. Biomol. NMR 4*, 727–734.

(21) Delaglio, F., Grzesiek, S., Vuister, G. W., Zhu, G., Pfeifer, J., and Bax, A. (1995) NMRPipe: A multidimensional spectral processing system based on UNIX pipes. *J. Biomol. NMR 6*, 277–293.

(22) Wishart, D. S., Sykes, B. D., and Richards, F. M. (1992) The chemical shift index: A fast and simple method for the assignment of protein secondary structure through NMR spectroscopy. *Biochemistry 31*, 1647–1651.

(23) Farrow, N. A., Zhang, O., Forman-Kay, J. D., and Kay, L. E. (1995) Comparison of the backbone dynamics of a folded and an unfolded SH3 domain existing in equilibrium in aqueous buffer. *Biochemistry 34*, 868–878.

(24) Clore, G. M., Szabo, A., Bax, A., Kay, L. E., Driscoll, P. C., and Gronenborn, A. M. (1990) Deviations from the Simple Two-Parameter Model-Free Approach to the Interpretation of Nitrogen-15 Nuclear Magnetic Relaxation of Proteins. *J. Am. Chem. Soc. 112*, 4989–4991.

(25) Kay, L. E., Torchia, D. A., and Bax, A. (1989) Backbone dynamics of proteins as studied by ^{15}N inverse detected heteronuclear NMR spectroscopy: Application to staphylococcal nuclease. *Biochemistry 28*, 8972–8979.

(26) Lipari, G., and Szabo, A. (1982) Model-Free Approach to the Interpretation of Nuclear Magnetic Resonance Relaxation in Macromolecules. 1. Theory and Range of Validity. *J. Am. Chem. Soc. 104*, 4546.

(27) Mandel, A. M., Akke, M., and Palmer, A. G.III (1995) Backbone dynamics of *Escherichia coli* ribonuclease HI: Correlations with structure and function in an active enzyme. *J. Mol. Biol. 246*, 144–163.

(28) Dosset, P., Hus, J. C., Marion, D., and Blackledge, M. (2001) A novel interactive tool for rigid-body modeling of multi-domain macromolecules using residual dipolar couplings. *J. Biomol. NMR 20*, 223–231.

(29) Tjandra, N., Feller, S. E., Pastor, R. W., and Bax, A. (1995) Rotational Diffusion Anisotropy of Human Ubiquitin from ^{15}N NMR Relaxation. *J. Am. Chem. Soc. 117*, 12562–12566.

(30) Pawley, N. H., Wang, C., Koide, S., and Nicholson, L. K. (2001) An improved method for distinguishing between anisotropic tumbling and chemical exchange in analysis of ^{15}N relaxation parameters. *J. Biomol. NMR 20*, 149–165.

(31) Bai, Y., Milne, J. S., Mayne, L., and Englander, S. W. (1993) Primary structure effects on peptide group hydrogen exchange. *Proteins 17*, 75–86.

(32) Zhang, Y.-Z. Protein and peptide structure and interactions studied by hydrogen exchange and NMR. Ph.D. Thesis, Structural Biology and Molecular Biophysics, University of Pennsylvania, PA, USA.

(33) Kim, K. S., Fuchs, J. A., and Woodward, C. K. (1993) Hydrogen exchange identifies native-state motional domains important in protein folding. *Biochemistry 32*, 9600–9608.

(34) DeLano, W. L. (2002) The PyMOL Molecular Graphics System, DeLano Scientific, San Carlos, CA.

(35) Tsodikov, O. V., Record, M. T.Jr., and Sergeev, Y. V. (2002) Novel computer program for fast exact calculation of accessible and molecular surface areas and average surface curvature. *J. Comput. Chem. 23*, 600–609.

(36) Parsonage, D., Youngblood, D. S., Sarma, G. N., Wood, Z. A., Karplus, P. A., and Poole, L. B. (2005) Analysis of the link between enzymatic activity and oligomeric state in AhpC, a bacterial peroxiredoxin. *Biochemistry 44*, 10583–10592.
(37) Ramsay, G. D., and Eftink, M. R. (1994) Analysis of multidimensional spectroscopic data to monitor unfolding of proteins. *Methods Enzymol. 240*, 615–645.
(38) Hvidt, A., and Nielsen, S. O. (1966) Hydrogen exchange in proteins. *Adv. Protein Chem. 21*, 287–386.
(39) Jayaraman, B., and Nicholson, L. K. (2007) Thermodynamic dissection of the Ezrin FERM/CERMAD interface. *Biochemistry 46*, 12174–12189.
(40) Wagner, G. (1983) Characterization of the distribution of internal motions in the basic pancreatic trypsin inhibitor using a large number of internal NMR probes. *Q. Rev. Biophys. 16*, 1–57.
(41) Wildes, D., Anderson, L. M., Sabogal, A., and Marqusee, S. (2006) Native state energetics of the Src SH2 domain: Evidence for a partially structured state in the denatured ensemble. *Protein Sci. 15*, 1769–1779.
(42) Woodward, C., Carulla, N., and Barany, G. (2004) Native state hydrogen-exchange analysis of protein folding and protein motional domains. *Methods Enzymol. 380*, 379–400.
(43) Pace, C. N., Hebert, E. J., Shaw, K. L., Schell, D., Both, V., Krajcikova, D., Sevcik, J., Wilson, K. S., Dauter, Z., Hartley, R. W., and Grimsley, G. R. (1998) Conformational stability and thermodynamics of folding of ribonucleases Sa, Sa2 and Sa3. *J. Mol. Biol. 279*, 271–286.
(44) Carvalho, A. P., Fernandes, P. A., and Ramos, M. J. (2006) Similarities and differences in the thioredoxin superfamily. *Prog. Biophys. Mol. Biol. 91*, 229–248.
(45) Woodward, C. (1993) Is the slow exchange core the protein folding core? *Trends Biochem. Sci. 18*, 359–360.
(46) Jeng, M. F., Campbell, A. P., Begley, T., Holmgren, A., Case, D. A., Wright, P. E., and Dyson, H. J. (1994) High-resolution solution structures of oxidized and reduced *Escherichia coli* thioredoxin. *Structure 2*, 853–868.
(47) Katti, S. K., LeMaster, D. M., and Eklund, H. (1990) Crystal structure of thioredoxin from *Escherichia coli* at 1.68 Å resolution. *J. Mol. Biol. 212*, 167–184.
(48) Smeets, A., Evrard, C., Landtmeters, M., Marchand, C., Knoops, B., and Declercq, J. P. (2005) Crystal structures of oxidized and reduced forms of human mitochondrial thioredoxin 2. *Protein Sci. 14*, 2610–2621.
(49) Kelley, R. F., Shalongo, W., Jagannadham, M. V., and Stellwagen, E. (1987) Equilibrium and kinetic measurements of the conformational transition of reduced thioredoxin. *Biochemistry 26*, 1406–1411.
(50) Stone, M. J., Chandrasekhar, K., Holmgren, A., Wright, P. E., and Dyson, H. J. (1993) Comparison of backbone and tryptophan sidechain dynamics of reduced and oxidized *Escherichia coli* thioredoxin using ^{15}N NMR relaxation measurements. *Biochemistry 32*, 426–435.
(51) Jeng, M. F., and Dyson, H. J. (1995) Comparison of the hydrogen-exchange behavior of reduced and oxidized *Escherichia coli* thioredoxin. *Biochemistry 34*, 611–619.
(52) Kaminsky, S. M., and Richards, F. M. (1992) Differences in hydrogen exchange behavior between the oxidized and reduced forms of *Escherichia coli* thioredoxin. *Protein Sci. 1*, 10–21.
(53) Ren, B., Tibbelin, G., de Pascale, D., Rossi, M., Bartolucci, S., and Ladenstein, R. (1998) A protein disulfide oxidoreductase from the archaeon *Pyrococcus furiosus* contains two thioredoxin fold units. *Nat. Struct. Biol. 5*, 602–611.
(54) Giuliani, M. C., Tron, P., Leroy, G., Aubert, C., Tauc, P., and Giudici-Orticoni, M. T. (2007) A new sulfurtransferase from the hyperthermophilic bacterium *Aquifex aeolicus*. Being single is not so simple when temperature gets high. *FEBS J. 274*, 4572–4587.
(55) Tanaka, Y., Tsumoto, K., Yasutake, Y., Umetsu, M., Yao, M., Fukada, H., Tanaka, I., and Kumagai, I. (2004) How oligomerization contributes to the thermostability of an archaeon protein. Protein L-isoaspartyl-O-methyltransferase from *Sulfolobus tokodaii*. *J. Biol. Chem. 279*, 32957–32967.
(56) Vieille, C., and Zeikus, G. J. (2001) Hyperthermophilic enzymes: Sources, uses, and molecular mechanisms for thermostability. *Microbiol. Mol. Biol. Rev. 65*, 1–43.
(57) Zavodszky, P., Kardos, J., Svingor, Á., and Petsko, G. A. (1998) Adjustment of conformational flexibility is a key event in the thermal adaptation of proteins. *Proc. Natl. Acad. Sci. U.S.A. 95*, 7406–7411.